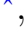


# The *NuSTAR* view of the non-thermal emission from PSR J0437–4715

S. Guillot<sup>1,2</sup> , V. M. Kaspi<sup>2</sup>, R. F. Archibald<sup>2</sup>, M. Bachetti<sup>3</sup>, C. Flynn<sup>4</sup>, F. Jankowski<sup>4</sup>, M. Bailes<sup>4</sup>, S. Boggs<sup>5</sup>, F. E. Christensen<sup>6</sup>, W. W. Craig<sup>6,7</sup>, C. A. Hailey<sup>8</sup>, F. A. Harrison<sup>9</sup>, D. Stern<sup>10</sup>, W. W. Zhang<sup>11</sup>

<sup>1</sup> Instituto de Astrofísica, Facultad de Física, Pontificia Universidad Católica de Chile, Av. Vicuña Mackenna 4860, 782-0436 Macul, Santiago, Chile

<sup>2</sup> Department of Physics and McGill Space Institute, McGill University, 3600 rue University Montréal, QC, Canada H3A-2T8

<sup>3</sup> Osservatorio Astronomico di Cagliari, via della Scienza 5, 09047 Selargius, Italy

<sup>4</sup> Centre for Astrophysics and Supercomputing and ARC Centre for All-Sky Astrophysics (CAASTRO),

Swinburne University of Technology, Post Office Box 218 Hawthorn, VIC 3122, Australia.

<sup>5</sup> Space Sciences Laboratory, University of California, Berkeley, CA 94720, USA

<sup>6</sup> DTU Space, National Space Institute, Technical University of Denmark, Elektrovej 327, DK-2800 Lyngby, Denmark

<sup>7</sup> Lawrence Livermore National Laboratory, Livermore, CA 94550, USA

<sup>8</sup> Columbia Astrophysics Laboratory, Columbia University, New York, NY 10027, USA

<sup>9</sup> Space Radiation Laboratory, California Institute of Technology, 1200 E California Blvd, MC 249-17, Pasadena, CA 91125, USA

<sup>10</sup> Jet Propulsion Laboratory, California Institute of Technology, Pasadena, CA 91109, USA

<sup>11</sup> NASA Goddard Space Flight Center, Astrophysics Science Division, Code 661, Greenbelt, MD 20771, USA

6 March 2022

## ABSTRACT

We present a hard X-ray *NuSTAR* observation of PSR J0437–4715, the nearest millisecond pulsar. The known pulsations at the apparent pulse period  $\sim 5.76$  ms are observed with a significance of  $3.7\sigma$ , at energies up to 20 keV above which the *NuSTAR* background dominates. We measure a photon index  $\Gamma = 1.50 \pm 0.25$  (90% confidence) for the power law fit to the non-thermal emission. It had been shown that spectral models with two or three thermal components fit the *XMM-Newton* spectrum of PSR J0437–4715, depending on the slope of the power-law component, and the amount of absorption of soft X-rays. The new constraint on the high-energy emission provided by *NuSTAR* removes ambiguities regarding the thermal components of the emission below 3 keV. We performed a simultaneous spectral analysis of the *XMM-Newton* and *NuSTAR* data to confirm that three thermal components and a power law are required to fit the 0.3–20 keV emission of PSR J0437–4715. Adding a *ROSAT*-PSPC spectrum further confirmed this result and allowed us to better constrain the temperatures of the three thermal components. A phase-resolved analysis of the *NuSTAR* data revealed no significant change in the photon index of the high-energy emission. This *NuSTAR* observation provides further impetus for future observations with the *NICER* mission (*Neutron Star Interior Composition Explorer*) whose sensitivity will provide much stricter constraints on the equation of state of nuclear matter by combining model fits to the pulsar’s phase-folded lightcurve with the pulsar’s well-defined mass and distance from radio timing observations.

**Key words:** (stars:) pulsars: individual: PSR 0437–4715, stars: neutron

## 1 INTRODUCTION

PSR J0437–4715 (J0437, hereafter), currently the nearest millisecond pulsar (MSP) to the Earth, was discovered in the

70 cm Parkes radio pulsar survey (Johnston et al. 1993) and subsequently in the X-rays with *ROSAT* (Becker & Trümper 1993). Since then, it has been extensively studied in multiple energy bands. Radio observations allow precise measurements of the pulsar spin ( $P = 5.76$  ms), intrinsic spin-down rate ( $\dot{P} = 5.8 \times 10^{-20} \text{ s s}^{-1}$ ), binary system orbital properties

\* email: sguillot@astro.puc.cl

(Verbiest et al. 2008), as well as the distance  $156.3 \pm 1.3$  pc (Deller et al. 2008). In the infrared and optical bands, the emission from the white dwarf companion dominates, leading to constraints on its properties (Durant et al. 2012). J0437 has also been detected in the near and far ultraviolet (UV), where the Rayleigh-Jeans tail of the pulsar surface thermal emission is thought to dominate the thermal emission of the white dwarf companion (Durant et al. 2012). Previous *XMM-Newton* fast-timing mode observations of J0437 have permitted the interpretation of the phase-modulated soft X-ray flux as the thermal emission from two polar caps moving in and out of the line of sight as the pulsar rotates (Bogdanov 2013). Observations with the *Fermi Gamma-Ray Space Telescope* have also detected  $> 100$  MeV pulsed emission from J0437, thought to originate far from the neutron star (NS) surface (Abdo et al. 2009).

However, because of its faintness in the hard X-ray band ( $\sim 5$ – $100$  keV), as well as its proximity on the sky ( $\sim 4'$ ) to the bright active galactic nucleus RX J0437.4-4711 (Halpern et al. 1996), the emission of J0437 in this band has been inaccessible to the previous generation of hard X-ray telescopes, such as *INTEGRAL* (Winkler et al. 2003) or the *Swift* Burst Alert Telescope (Krimm et al. 2013). The MOS detectors of *XMM-Newton* cover part of the hard X-ray band ( $\lesssim 10$  keV), but the drop in effective area above 4 keV limits the constraints on the high energy tail of the spectrum (Bogdanov 2013). When it was launched, the *Nuclear Spectroscopic Telescope Array* (*NuSTAR*), with its hard X-ray focusing optics capabilities, opened a new window on the hard X-ray sky (Harrison et al. 2013), with unrivalled sensitivity in the 3–79 keV range. In addition, the angular resolution of *NuSTAR* (18 arcseconds full-width half-maximum) allows us to obtain the high-energy spectrum of J0437 without the contaminating photons from the nearby active galactic nucleus.

With the *XMM* observations, phase-averaged (with *XMM-mos*) and pulse phase-resolved (with *XMM-pn* in fast-timing mode) analyses were used to determine the system geometry and to characterize the surface emission (Bogdanov 2013, using the method presented in Bogdanov et al. 2008). In turn, these analyses led to some constraints on the compactness of the pulsar  $M_{\text{NS}}/R_{\text{NS}}$ . The independently measured mass,  $M_{\text{NS}} = 1.76 \pm 0.20 M_{\odot}$  from radio timing (Verbiest et al. 2008), therefore restricted the range of possible radii to values  $\gtrsim 11.1$  km. Recent radio timing measurements of J0437 have led to a mass estimate of  $M_{\text{NS}} = 1.44 \pm 0.07 M_{\odot}$  (Reardon et al. 2016), which would allow slightly lower radii according to the analysis of Bogdanov (2013).

Measurements of the NS radii are crucial to determine their interior properties, and study the behavior of dense nuclear matter (e.g., Lattimer & Prakash 2007; Heinke 2013; Miller 2013, for reviews). Specifically, the equation of state of matter at and above nuclear density can only be determined by observations of NSs, and in particular, measurements of their radii. In addition to the pulse profile modeling of millisecond pulsars, other methods exist to measure the NS radius, including constraints from the photospheric radius expansion bursts of type I X-ray bursting NSs (e.g., Özel & Psaltis 2009; Güver et al. 2010; Suleimanov et al. 2011; Özel et al. 2016), and the measurement of  $R_{\text{NS}}$  from the surface emission of NSs in quiescent low-mass X-ray binaries (Webb

**Table 1.** Selected X-ray Observations of PSR J0437–4715

ObsID	Telescope/ Instrument	Start Time (UT)	Usable Exposure (ksec)
701184	<i>ROSAT</i> -PSPC	1992-09-20 17:51:32	6.1
0603460101	<i>XMM</i> -mos1	2009-12-15 19:41:16	118.2
0603460101	<i>XMM</i> -mos2	2009-12-15 19:41:16	119.3
0603460101	<i>XMM</i> -pn	2009-12-15 20:00:24	117.0
30001061002	<i>NuSTAR</i> -FPMA	2014-12-29 14:51:07	78.8
30001061002	<i>NuSTAR</i> -FPMB	2014-12-29 14:51:07	78.8
30001061004	<i>NuSTAR</i> -FPMA	2014-12-31 18:26:07	68.4
30001061004	<i>NuSTAR</i> -FPMB	2014-12-31 18:26:07	68.4
30001061006	<i>NuSTAR</i> -FPMA	2015-01-02 17:16:07	67.9
30001061006	<i>NuSTAR</i> -FPMB	2015-01-02 17:16:07	67.9

& Barret 2007; Heinke et al. 2006, 2014; Guillot et al. 2011, 2013; Guillot & Rutledge 2014). However, all methods are affected by systematic uncertainties and it is important to understand and test them all until they converge to consistent results.

For J0437, the measurement of the compactness (i.e., radius measurement) relies on observations of the pulsed thermal surface emission. However, it has been shown that the poorly constrained high-energy tail, modeled with a power law (PL), affects how well the thermal emission can be constrained (Bogdanov 2013). Specifically, depending on the PL index, two or three thermal components were necessary to fit the soft X-ray emission of J0437: with a softer PL index  $\sim 2.5$ , the third thermal component ( $kT_{\text{eff}} \sim 50$  keV) is unnecessary. This can be explained by the fact that a PL with  $\Gamma \sim 2.5$  fitted to the high-energy tail starts dominating the emission in the 0.1–0.3 keV range where the fluxes from the two hottest thermal components (corresponding to the spot emission) decline. On the other hand, a harder PL with  $\Gamma \sim 1.5$  leaves an excess of counts in the 0.1–0.3 keV band which is then well fit by a cold thermal component.

Since the constraints on  $M_{\text{NS}}/R_{\text{NS}}$  are extracted from the pulse profile and the thermal components normalizations, the poorly constrained PL limits the precision of the  $M_{\text{NS}}/R_{\text{NS}}$  measurement. In other words, an independent measurement of the PL index can provide a better constraint on the thermal components and therefore on the radius of J0437. This is of particular importance since this MSP is the primary target for the upcoming *Neutron Star Interior Composition Explorer* (*NICER*, Gendreau et al. 2012, expected launch date: early 2017). The large effective area of this future mission mounted on the International Space Station will collect  $\sim 10^6$  photons from J0437 (amongst other NSs) for the sole purpose of analyzing its pulsed emission and measuring its compactness. It is therefore crucial to know and constrain, ahead of time, the nature of the high energy emission of this key *NICER* target.

This paper presents a *NuSTAR* observation of J0437, as well as a joint analysis with archival *XMM* observations. Analysis of an archival *ROSAT*-PSPC observation complements the *XMM*-MOS data by providing an energy coverage to lower energies. Combined with the *NuSTAR* observation, the spectral data presented in this work cover an energy range from 0.1 keV to 20 keV. In Section 2, the observations are described together with the data reduction and analysis procedures. The results of the timing and spectral analysis are presented in Sections 3 and 4, respectively. Finally, Section 5 summarizes and discusses the results.

## 2 OBSERVATIONS AND ANALYSIS

### 2.1 *NuSTAR* observations

The *NuSTAR* Observatory consists of two co-aligned telescopes focusing hard X-rays in the 3–79 keV range onto two focal planes modules, FPMA and FPMB (Harrison et al. 2013). It provides relatively low-background imaging capabilities (18'' full-width half-maximum) in the hard X-ray band with a 2  $\mu$ sec relative timing resolution.

A  $\sim 200$  ks (total on source) observation of J0437 was performed in Dec./Jan. 2015 (see Table 1). The FPMA and FPMB data were re-processed following the standard pipeline of the *NuSTAR* data analysis system, *nupipeline* v0.4.3 and *heasoft* v16.0, together with the *NuSTAR* calibration files from *CALDB* v4.6.8. During the data processing, photon time tags were barycentered to the Solar system reference frame using the position of J0437 obtained from radio timing.

For the spectral analysis, the size of the circular extraction region was chosen to maximize the signal-to-noise ratio (S/N). Specifically, a range of source extraction radii were tested between 10'' and 120'', with various annuli around the source regions for the backgrounds. A 35'' circular source region maximizes the S/N and was therefore used to generate the spectra. For the background, an annulus region with inner radius 80'' and outer radius of 87.2'' was used to ensure that both the source and background regions have the same area. Because the background noise dominates the source signal above 20 keV, counts above that energy are discarded, restricting the spectral analysis to the 3–20 keV energy range. The background subtracted count rates for J0437 are  $1.50 \pm 0.15$  counts/ksec for FPMA and  $1.60 \pm 0.16$  counts/ksec for FPMB, in the 3–20 keV energy range. Data from each module were combined to generate one spectrum for each module (including the response files), and following that step, photon events were grouped with a minimum of 40 counts per bin. Note that the FPMA and FPMB spectra are not combined together. Instead a cross-normalization constant between them is used during the spectral analysis to account for cross-calibration uncertainties between the two modules (see Section 4.1).

### 2.2 *XMM-Newton* observations

This work used a continuous 130 ks archival observation of J0437 whose analysis was presented in detail in a previous work (Bogdanov 2013). The fast readout cadence (30  $\mu$ sec) of the European Photon Imaging Camera (EPIC) pn instrument in timing mode allowed the measurement of the pulse profile of J0437, while the EPIC MOS1 and MOS2 instruments were used for the spectral analysis. In this work, the raw pn and MOS data were reprocessed with the *pnchain* and *emchain* tasks of the *XMMSAS* v14.0 package and with the latest calibration files, following the standard data reduction and analyses procedures. As in Bogdanov (2013), the time intervals of high background were removed leading to the exposure times listed in Table 1. For the MOS1/2 imaging data, circular extraction regions were used with 60'' radii for the source regions. The MOS1/2 spectra were generated in the 0.3–10 keV band since the calibration below 0.3 keV is unreliable. Specifically, quantum efficiency inhomogeneities in the detector itself are present at low energy

(see *XMM* calibration document CAL-TN-0018<sup>1</sup>), and are not considered in the *XMMSAS* (priv. comm., J. Ebrero, *XMM-Newton* Science Operation Center). For all spectra, the response matrix and ancillary response files were obtained with the tools *rmfgen* and *arfgen*, respectively. The MOS1 and MOS2 spectra (extracted with identical parameters) and their response files were combined into a single spectrum using the task *epicspeccombine*, and events were then binned with a minimum of 100 counts per bin. Overall, the data reduction of the *XMM* data was very similar to that of Bogdanov (2013), except for the energy range used.

A 2002 observation of J0437 with *XMM* is also publicly available. However, the X-ray flux decreased by  $\sim 5\%$  between 2002 and 2009. This decrease was measured by fitting the spectra of both epochs with the same model, except for a multiplicative constant (fixed to unity for the 2002 data, and free to vary for the 2009 data). We found a statistically acceptable fit, and a multiplicative constant  $c = 0.945 \pm 0.014$  (90% confidence). We note that an accumulation of contaminants on the MOS detectors since the launch of *XMM* have affected the sensitivity in the low-energy range<sup>2</sup>. However, this effect has been accounted for in the publicly-available *XMM* calibration files since *XMMSAS* v13.5. It is beyond the scope of this paper to present a detailed analysis of the soft X-ray variability of J0437. We therefore choose to use only the longest and most recent observation of this MSP, and we leave it for future work to investigate the origin of this possible soft X-ray variability.

### 2.3 *ROSAT*-PSPC observations

This work also took advantage of the energy response of the *ROSAT*-PSPC camera down to 0.1 keV. Using pre-processed data sets, the spectral extraction was performed with the *ftools* package *xselect*. Source counts were selected with a circular region centered around the radio position of J0437, with a radius of 70''. For the background, a source-centered annulus was chosen, with inner radius 70'' and outer radius 110''. The response matrix file is provided by *CALDB*<sup>3</sup> and the ancillary response file with the *ftools* command *pcarf*. Channels were grouped with a minimum of 40 counts per bin.

## 3 TIMING ANALYSIS

To study the 2.0–20 keV *NuSTAR* pulse profile of J0437, the barycentered photon event times were folded using the radio ephemeris, obtained at the Molonglo Observatory (see Appendix A), with the *photon* plugin<sup>4</sup> of the TEMPO2 pulsar timing package (Edwards et al. 2006). The phases obtained from folding were then grouped into 10 phase bins,

<sup>1</sup> Available at <http://www.cosmos.esa.int/web/xmm-newton/calibration-documentation>

<sup>2</sup> see *XMM* calibration document CAL-SRN-0305 available at <http://xmm2.esac.esa.int/docs/documents/CAL-SRN-0305-1-0.ps.gz>

<sup>3</sup> Available at [https://heasarc.gsfc.nasa.gov/docs/rosat/pspc\\_matrices.html](https://heasarc.gsfc.nasa.gov/docs/rosat/pspc_matrices.html)

<sup>4</sup> by Anne Archibald, based on Lucas Guillemot's *Fermi* plugin.

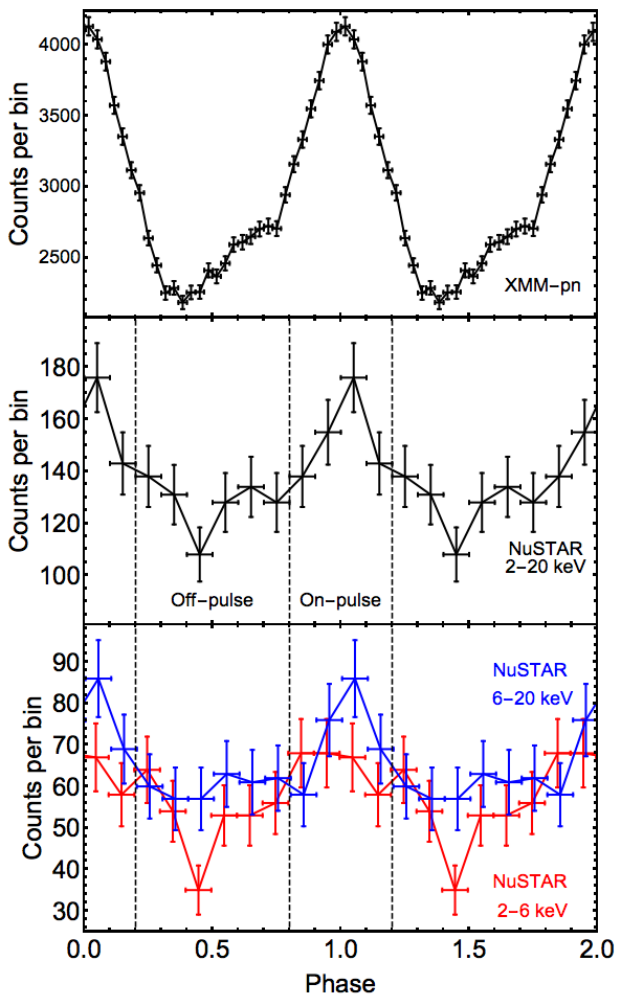


**Figure 1.** (*top*) XMM-pn pulse profile of PSR J0437–4715 in the 0.5–2.0 keV energy range, as analysed in [Bogdanov \(2013\)](#). (*middle*) NuSTAR pulse profile of PSR J0437–4715 obtained by folding photons in the 2–20 keV band at the known radio ephemeris. The H-test probability associated with this pulse profile is 0.00022 ( $\sim 3.7\sigma$ ). The vertical dashed lines separate the on- and off-pulse regions used to generate the phase-resolved spectra presented in Section 4.3. (*bottom*) 2–6 keV and 6–20 keV NuSTAR pulse profiles of PSR J0437–4715. When the photons are split into two energy bands, the pulsation detection significance diminishes (see text) due to the decrease in S/N. Note that the pulse profiles of PSR J0437–4715 observed by NuSTAR might be distorted from the true morphology by the NuSTAR clock drift (see Section 3.1).

with Poisson errors in each bin (Figure 1). An H-test was performed to evaluate the significance of the observed pulse ([de Jager et al. 1989](#)). We found an H-test probability of 0.00022, which quantifies the significance of the H-value by estimating the probability of obtaining, by chance, an H-value as large, or larger, from sampling a uniform distribution. The H-test probability found corresponds to a  $\sim 3.7\sigma$  significance. By separating photons from the on- and off-pulse parts of the profile (see divisions in Figure 1), spectra were obtained during these two different phases of the rotation. This is further discussed in Section 4.3.

The resulting pulsed fraction, defined as the fraction of

counts above the minimum<sup>5</sup>, of the J0437 profile is  $24 \pm 6\%$  ( $1\sigma$ , all pulse fraction errors provided thereafter are given at the  $1\sigma$  level), for photons in the energy range 2–20 keV. Note that NuSTAR is sensitive to photons below 3 keV, and while those photons cannot formally be used for a spectral analysis (due to the current absence of calibration below 3 keV), they were used here to study the pulse profile. When compared to the pulse fractions measured in the soft X-ray band with XMM ( $32 \pm 1\%$ ,  $35 \pm 1\%$ ,  $37 \pm 1\%$ ,  $37 \pm 1\%$ , and  $35 \pm 2\%$  in the 0.275–0.35, 0.35–0.55, 0.55–0.75, 0.75–1.1, and 1.1–1.7 keV bands, respectively, [Bogdanov 2013](#)), there appears to be a decrease in the pulsed fraction as energy increases. Photons were then split into two separate bands, 2–6 keV and 6–20 keV, before being folded with the method described in the previous paragraph. The separation energy is chosen to have similar number of photons in both bands. The pulse fractions in these two bands are:  $32 \pm 9\%$  and  $20 \pm 8\%$ , respectively. These pulse fractions are different from 0 at the 99.92% and 98.76% confidence level, respectively, which correspond to  $3.4\sigma$  and  $2.5\sigma$ . Although the S/N does not allow one to draw a firm conclusion, these values appear to reinforce the suggestion that the pulsed fraction decreases with increasing photon energy. We also note that although the detection of pulsations in the full 2–20 keV energy range is significant, the detection is only marginal in the two separate energy bands: the H-test probabilities are 0.0057 for the low energy band (equivalent to  $2.7\sigma$ ), and 0.015 for the high energy band (equivalent to  $2.4\sigma$ ).

It is important to keep in mind that the true morphology of the pulse profile might be distorted by a drift in the NuSTAR clock, causing a smearing of the pulse, and therefore a decrease in the measured pulsed fraction. The attempt to correct for the NuSTAR clock drift is discussed in Section 3.1 and the smearing of the pulse is quantified in Section 3.2.

### 3.1 Searching and correcting for the residual clock drift

The NuSTAR onboard photon time stamping clock is known to suffer drifts that are due to temperature variations as the telescope orbits the Earth and is exposed to a variable environment. The largest fraction of this clock drift can be corrected for during the processing of NuSTAR data with up-to-date *clock files*<sup>6</sup> provided by the NuSTAR calibration team. However, there remains a residual clock drift. Therefore, while the NuSTAR temporal resolution is  $2 \mu\text{s}$ , inaccuracies in the time stamping due to the clock drift limit the timing accuracy to  $\sim 0.5 \text{ ms}$ .

This residual clock drift has been noticed in observations of the Crab pulsar ([Madsen et al. 2015](#)). Residuals in the timing exhibited modulations at a period of  $\sim 97 \text{ min}$ ,

<sup>5</sup> This pulsed fraction estimator is used here for convenient comparison with the work of [Bogdanov 2013](#). Note that there is a possible bias toward higher pulse fraction with this estimator compared to the root-mean-square (RMS) pulsed fraction estimator ([An et al. 2015](#)). Nonetheless, for a small number of bins ( $\sim 10$  bins, as used in the present work), the bias compared to the RMS method appears to be minimal (see Fig. 12 of [An et al. 2015](#)).

<sup>6</sup> The NuSTAR clock file v050 was used in this analysis.



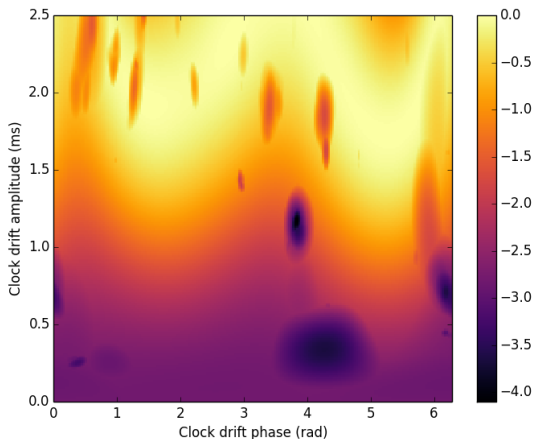


**Figure 2.** Results of the search for the *NuSTAR* clock drift using the pulse profile of PSR J0437–4715. The clock drift is assumed to be sinusoidal, with unknown phase and amplitude, and with a period equal to that of the *NuSTAR* orbit. The color scale corresponds to the H-score log-probability of such a score happening by chance (see Section 3.1).

the satellite’s orbital period. The detection of this residual clock drift in the timing analysis of the Crab pulsar was only possible because this source is bright enough that pulse time-of-arrivals can be obtained on timescales of  $\sim 5$  min, much shorter than the  $\sim 97$  min orbital period. The residual drifts of the photon time stamps cause a smearing of the otherwise sharper pulse. While this did not significantly affect the pulse shape of the Crab pulsar (spin period  $P = 33$  ms), the effects on a faint 5.76 ms pulse could be more dramatic.

At the count rates encountered in this *NuSTAR* observation of J0437 ( $\sim 800$  counts after background subtraction), the pulse shape could be severely affected by the clock drift. In an attempt to recover the true, unaltered, pulse shape of J0437, a search in amplitude and phase was performed for the residual clock drift, assuming that it follows a sinusoidal pattern. The exact amplitude (in milliseconds) of the time correction that needs to be applied to each photon is not well known; it was measured to be  $\sim 0.4 \pm 0.1$  ms from the Crab pulsar *NuSTAR* data (Madsen et al. 2015). In addition, the phase of the clock-drift modulation is unknown. Consequently, a grid search method in amplitude-phase ( $A, \phi$ ) was employed. For each pair of parameters, the following correction to the time stamp  $t_i$  of each photon  $i$  was applied:

$$\Delta t_i = A \sin \left( \frac{2\pi t_i}{P_{\text{orb}}} + \phi \right), \quad (1)$$

where  $P_{\text{orb}}$  is the satellite orbital period at the time of the observation, obtained from the orbit files. The time correction  $\Delta t_i$  can be converted into a correction  $\Delta \theta_i$  to the phase  $\theta_i$  of each photon, according to:

$$\Delta \theta_i = \frac{\Delta t_i}{P_{t_0, \text{J0437}} + \dot{P}_{t_0, \text{J0437}} (t_i - t_0)}, \quad (2)$$

where  $P_{\text{J0437}}$  and  $\dot{P}_{\text{J0437}}$  are the period and period derivative of J0437 at the reference time  $t_0$  (from the ephemeris).

Each pair of parameters ( $A, \phi$ ) therefore resulted in a corrected profile in which the significance of a pulse was in-

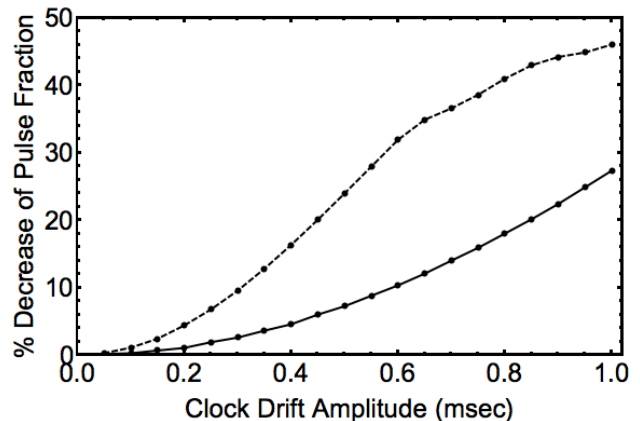


**Figure 3.** Fractional difference between the intrinsic pulsed fraction of a 5.76 ms sinusoidal pulse profile and the pulsed fraction of a pulse profile distorted by the *NuSTAR* clock drift, as a function of the clock drift amplitude. The solid line corresponds to a sinusoidal simulated pulse profile, and the dashed line corresponds to simulated narrow Gaussian pulse profile with a 10% duty cycle ( $1\sigma$  width). For a clock drift amplitude of 0.4 ms (Madsen et al. 2015), the measured pulsed fraction is artificially reduced by  $\sim 5\%$ , assuming a sinusoidal pulse profile, and by  $\sim 16\%$  for a short duty cycle profile.

vestigated using an H-test. From this search, a grid of H values was obtained, or equivalently, H-test probabilities that allows one to determine whether the corrections applied by each pair of parameters result in a detected/improved pulse for J0437. The clock drift amplitudes and phases were sampled in the ranges 0–2.5 ms (step of 0.0125 ms) and 0 –  $2\pi$  (step of  $\pi/200$ ), respectively. Figure 2 shows the H-test probabilities obtained from the grid-search. Low H-test probabilities (dark purple) correspond to peaks in the H-score. We found that none of the detected peaks gives an H-test probability significantly higher than that for the zero amplitude clock-drift correction. In particular, the peak at  $A \sim 1.2$  ms is likely to be a statistical coincidence since there is no evidence from the Crab pulsar timing that the clock drift amplitude is that large. However, the less-significant peak at  $A \sim 0.3$  ms is closer to the expected residual clock drift amplitude (see above, and Madsen et al. 2015), but the low significance of the improvement prevents us from making any firm conclusions. More importantly, the  $A \sim 0.3$  ms solution does not change significantly the pulsed fraction or the morphology of the pulse profile.

### 3.2 Effect of the residual clock drift on the pulsed fraction

To estimate the magnitude of the smearing effect on the observed pulse profile, we simulated photons randomly drawn from a pulse profile distribution (with  $P = P_{\text{J0437}} = 5.76$  ms) over a total time equal to the time span of our *NuSTAR* observation. The randomly drawn times of these photons were then modified by a small time difference equal to what the clock drift would cause, following Equation 1 (assuming  $\phi = 0.0$ ). After folding these clock-drift modified photon times at the period  $P = 5.76$  ms, the pulsed fraction of this constructed pulse profile was calculated. It was then compared to the pulsed fraction of the pulse profile ob-

tained before altering the photon times with the clock-drift effect. This process was repeated for a range of clock-drift amplitudes between 0.0 and 1.0 ms, and 100 times for each amplitude. Finally, we calculated the average difference between the intrinsic pulsed fraction and that affected by a clock drift. This simulation was performed for a purely sinusoidal pulse profile, as well as for a small duty cycle pulse profile – we used a Gaussian profile with  $1\sigma = 0.05P_{J0437}$ . The percent decreases of the pulse fractions in these two cases are shown in Figure 3. If the true residual clock drift of *NuSTAR* has an amplitude of 0.4 ms, as suggested by the observations of the Crab Pulsar (Madsen et al. 2015), and by the clock-drift search described in Section 3.1, the measured pulsed fraction is underestimated by about  $\sim 16\%$  in the case of a short duty cycle pulse profile, and by  $\sim 5\%$  in the case of a sinusoidal pulse profile. While this effect is currently buried in the statistical uncertainties for J0437, it can become significant with deeper observations, and for other bright MSPs with  $P_{\text{spin}} \lesssim 5$  ms. For example, faster pulsars, such as SAX J1808.4–3658 ( $P_{\text{spin}} = 2.5$  ms, Wijnands & van der Klis 1998), observed with *NuSTAR*, can expect to have their measured pulsed fraction biased by  $\sim 40\%$  due to a 0.4 ms clock drift, assuming a small duty cycle pulse profile.

#### 4 SPECTRAL ANALYSIS

As was reported in previous work, the spectrum of J0437 contains multiple components: two thermal components, and a non-thermal component modeled with a PL (Zavlin et al. 2002; Zavlin 2006; Durant et al. 2012; Bogdanov 2013). A third thermal component (with  $kT_{\text{eff}} \sim 40$  eV) has been suggested to fit the lowest energy range available in the *XMM*-MOS data (Bogdanov 2013). Furthermore, *Hubble Space Telescope* observations also seem to advocate for a third thermal component representing the cold emission from the NS surface, for which the Rayleigh-Jeans tail is detected in the far UV and appears in excess of the modeling of the white-dwarf companion atmosphere (Durant et al. 2012). The *NuSTAR* spectrum of J0437 complements the *XMM*-MOS spectra up to 20 keV range, and provides a useful handle on the non-thermal emission. However, because the *NuSTAR* and *XMM* observations were obtained at a different epoch, the joint analysis described below assumes that J0437 is a non-variable source. This assumption is based on the lack of evidence for long term variability of the thermal emission in non-accreting MSPs like J0437 (Kaspi et al. 2006).

##### 4.1 *NuSTAR* spectroscopy

The analysis of the *NuSTAR* data was first performed without the *XMM*-MOS data. In the 3–20 keV range covered by *NuSTAR*, the non-thermal component dominates the emission, and a simple unabsorbed PL spectral model was used. Absorption of X-rays by the Galactic interstellar medium in that energy range plays a negligible role. A multiplicative constant  $c$ , fixed to unity for the FPMA spectrum and fitted for the FPMB spectrum, was added to take into account the cross-correlation uncertainties between the two modules. All following parameters resulting from the spectral analyses are quoted with 90% confidence. The photon

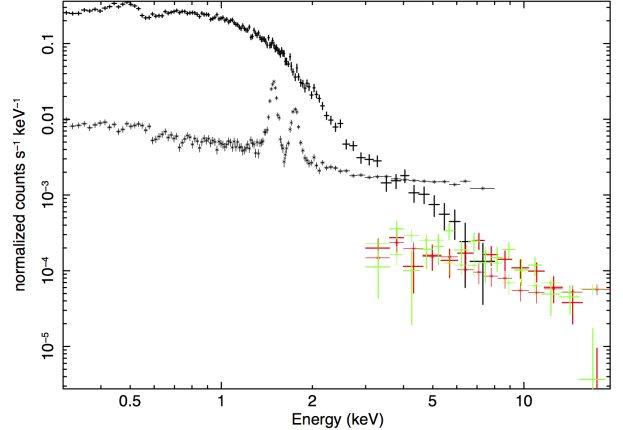


**Figure 4.** *XMM*-MOS (black), *NuSTAR*-FPMA (red) and *NuSTAR*-FPMB (green) count spectra of PSR J0437–4715 (data points with thick lines), together with their respective background spectra ('x' data points with thin error bars).

index measured is  $\Gamma = 1.60 \pm 0.25$ , consistent with, but significantly restricting the range of values previously tested or reported (Durant et al. 2012; Bogdanov 2013). The multiplicative constant is consistent with unity,  $c = 1.17^{+0.28}_{-0.23}$ . Adding a hot  $kT = 260$  eV blackbody (as observed in the *XMM*-MOS data analysis of Bogdanov 2013) with a fixed temperature and free normalization did not result in any significant change in the photon index.

##### 4.2 Joint spectral analysis

This subsection concerns the joint fit of the *XMM*-MOS and *NuSTAR* spectra. Figure 4 shows the count spectra obtained with *XMM*-MOS and *NuSTAR*, together with their respective backgrounds.

In the previous work, the low S/N of the *XMM*-MOS data at energies above  $\sim 3$  keV allowed the measured PL component to have indices in the range  $\sim 0.8 - 2.9$  at the 90% confidence level (Durant et al. 2012; Bogdanov 2013), depending on the number and types of the thermal components fitting the soft X-ray emission. Specifically, two or three thermal components both led to statistically acceptable fits, but resulted in different PL photon indices. Omitting the third (coldest) thermal component could be compensated for by a soft PL (higher  $\Gamma$ ) which would dominate the very-soft emission and account for the excess of counts in the softest energy band ( $< 0.3$  keV). We note that this emission at  $E < 0.3$  keV is detected in the *XMM*-MOS data (Bogdanov 2013), but in an energy band where the spectral calibration is undetermined.

Constraints on the non-thermal emission from the *NuSTAR* data therefore permit differentiation between the range of possible soft X-ray emission models proposed. The *NuSTAR* spectrum was simultaneously fit with the *XMM*-MOS spectrum. As performed above, a multiplicative constant  $c$  was used to account for cross-correlation uncertainties between the MOS (fixed  $c$ ) and the FPMA/B spectra (one fitted  $c$  parameter for each module). In this section, blackbody components were used for the thermal emission. Sec-

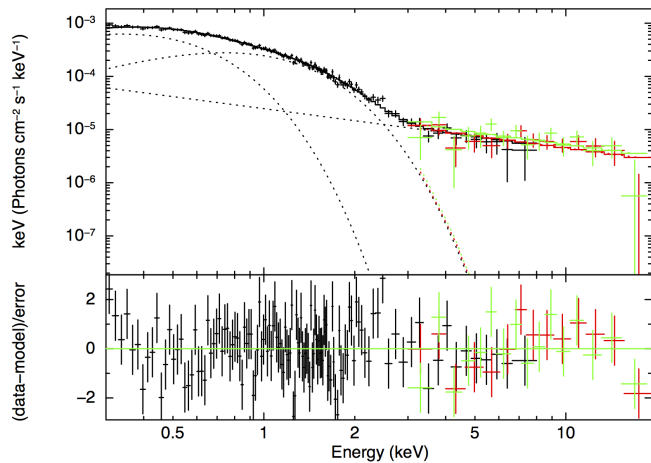


**Figure 5.** *XMM*-MOS (black), *NuSTAR*-FPMA (red) and *NuSTAR*-FPMB (green) unfolded spectra of PSR J0437–4715 fitted with an absorbed double-blackbody plus power-law model. While the fit is statistically acceptable, some structure in the residuals can be seen below 1 keV.

tion 5 discusses the use of NS atmosphere models to describe the hot spot emission and demonstrates that the choice of atmosphere model or Planck spectrum does not significantly affect the measured PL index. Finally, the Galactic absorption was quantified with the column density of hydrogen  $N_{\text{H}}$  (noted  $N_{\text{H},20}$  thereafter, when expressed in units of  $10^{20} \text{ atoms cm}^{-2}$ ). It was modeled using the *phabs* model, with the *bcmc* cross-sections (Balucinska-Church & McCammon 1992) and the *wilm* abundances (Wilms et al. 2000). Alternative abundances have also been tested, as well as the *tbabs* absorption model. The fits were insensitive to these changes: all parameters were consistent well within the  $1\sigma$  uncertainties of the values obtained with *phabs* and *wilm*.

As found in the previous work, the models `blackbody+powerlaw` and `blackbody+blackbody` are not statistically acceptable fits to present data. The former, with a null hypothesis probability  $p \sim 10^{-6}$ , presents highly structured residuals, especially above 6 keV. The latter has  $p \sim 10^{-45}$ , and does not fit any of the high energy emission above 3 keV. Considering the spectral model `blackbody+blackbody+powerlaw` (2BB+PL hereafter) resulted in a statistically acceptable fit (Figure 5), with  $\chi^2_{\nu}/\text{dof}$  (prob.) = 1.13/147 (0.13), and with a PL photon index  $\Gamma = 1.75 \pm 0.25$ . In this case, the hydrogen column density remains unconstrained,  $N_{\text{H},20} < 0.3$ , and consistent with zero.

The two multiplicative constants used for the two *NuSTAR* spectra are consistent with unity:  $c_{\text{FPMA}} = 1.03^{+0.25}_{-0.21}$  and  $c_{\text{FPMB}} = 1.20^{+0.28}_{-0.24}$ . Because of the low S/N, the multiplicative constants have large error bars, but they are nonetheless consistent with those obtained with the high-S/N data of *NuSTAR* calibration sources (Madsen et al. 2015). To investigate the possibility that the large value of  $c_{\text{FPMB}}$  is skewing the results, we performed a fit by fixing the multiplicative constant between FPMA and FPMB to 1.03, the typical value measured with the calibration sources (Madsen et al. 2015); a single free multiplicative constant

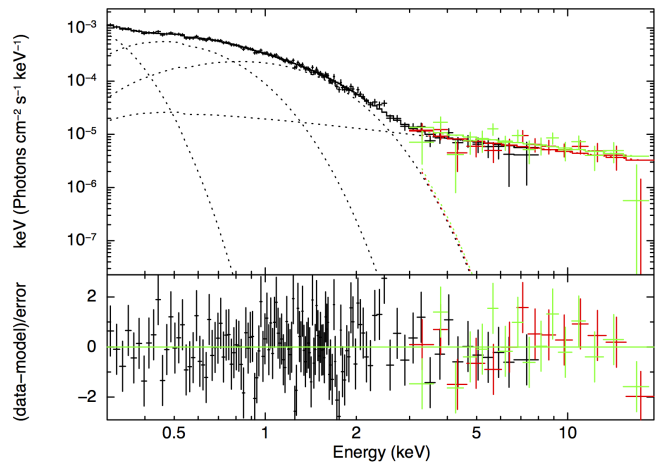


**Figure 6.** *XMM*-MOS (black), *NuSTAR*-FPMA (red) and *NuSTAR*-FPMB (green) unfolded spectra of PSR J0437–4715 fitted with an absorbed triple-blackbody plus power-law model. The addition of a third thermal component improves the fit ( $f$ -test probability of 0.0009), and improves the residuals below 1 keV compared to Figure 5.

between *XMM* and the *NuSTAR* detectors is still fitted to account for cross-calibration uncertainties between the two observatories. In this exercise<sup>7</sup>, the parameters changed by  $< 0.5\%$ , i.e., they are all consistent well within the uncertainties presented in Table 2. This indicates that the results are not skewed by the fitted multiplicative constants.

The temperatures of the two blackbodies obtained with the 2BB+PL model are consistent with those of the two hottest blackbodies in the three blackbody case of Bogdanov (2013). It is important to note that in the present analysis, the 0.1–0.3 keV range, where the coldest thermal component dominates, is excluded due to the lack of calibration of the *XMM*-MOS detector below 0.3 keV.

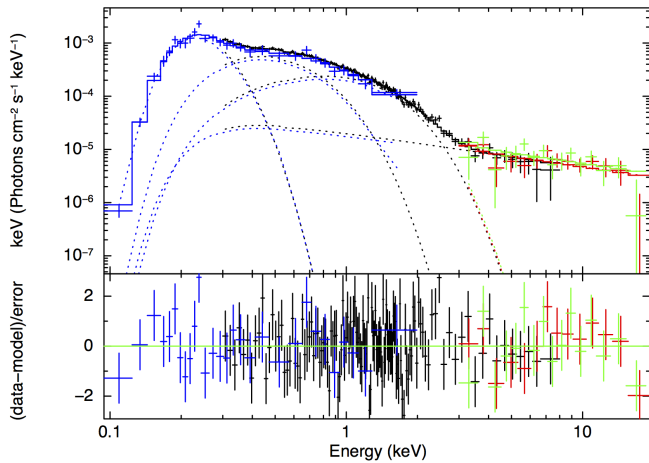
Nonetheless, adding a third thermal component in the present analysis improved the statistics:  $\chi^2_{\nu}/\text{dof}$  (prob.) = 1.04/145 (0.34). The  $f$ -test gives a probability of 0.0009 of the  $\chi^2$  improvement happening by chance when adding the thermal blackbody. The temperature of this added component is  $kT_{\text{eff}} = 34^{+54}_{-14} \text{ eV}$ , consistent with the value reported previously (Bogdanov 2013) using the MOS data down to 0.1 keV. This new fit improves the residuals in the lowest energy bins: 0.3–0.35 keV (Figure 6), but results in a poorly constrained temperature because of the limited energy range where this cold thermal component dominates. Therefore, this fit indicates that the third thermal component, emitted by the NS surface, likely exists. However, because of the lack of calibration, it is not recommended to include the 0.1–0.3 keV MOS data to better constrain this cold thermal emission and draw any firm conclusions.

To further investigate this, the *ROSAT*-PSPC data, and its calibrated spectral information down to 0.1 keV, proved a useful addition to the joint spectral analysis presented

<sup>7</sup> We performed the same exercise on the *NuSTAR* data alone (Section 4.1). The PL index was the same, and the PL normalization was 5% larger, but still consistent with that of Table 2.

**Table 2.** Phase-averaged Spectral Analysis of PSR J0437–4715

Spectral Model	$N_{\text{H},20}$	$kT_1$ (eV)	$R_{\text{eff},1}$ (km)	$kT_2$ (eV)	$R_{\text{eff},2}$ (km)	$kT_3$ (eV)	$R_{\text{eff},3}$ (km)	$\Gamma_{\text{PL}}$	$N_{\text{PL}}^a$	$\chi^2_{\nu}/\text{dof}$ (n.h.p)	$f$ -test probability $b$
<b><i>NuSTAR</i> FPMA/B</b>											
PL <sup>c</sup>	–	–	–	–	–	–	–	$1.60 \pm 0.25$	$1.9^{+1.3}_{-0.8}$	1.02/27 (0.43)	–
<b><i>XMM</i>-MOS1/2 + <i>NuSTAR</i> FPMA/B</b>											
2 BB+PL <sup>d</sup>	< 0.3	–	–	$120 \pm 6$	$0.25^{+0.03}_{-0.02}$	$262 \pm 10$	$0.051^{+0.006}_{-0.005}$	$1.75 \pm 0.25$	$2.5^{+1.2}_{-0.8}$	1.14/147 (0.13)	–
3 BB+PL <sup>e</sup>	< 8.9	$34^{+54}_{-14}$	$11^{+55}_{-7}$	$124^{+50}_{-12}$	$0.24^{+0.21}_{-0.13}$	$270^{+40}_{-13}$	$0.046^{+0.009}_{-0.016}$	$1.65 \pm 0.25$	$2.1^{+1.0}_{-0.7}$	1.04/145 (0.34)	0.0009
<b><i>ROSAT</i>-PSPC + <i>XMM</i>-MOS1/2 + <i>NuSTAR</i> FPMA/B</b>											
2 BB+PL <sup>d</sup>	< 0.6	–	–	$111^{+5}_{-6}$	$0.26^{+0.05}_{-0.09}$	$250 \pm 7$	$0.056^{+0.006}_{-0.005}$	$2.15^{+0.55}_{-0.20}$	$4.5^{+4.6}_{-0.4}$	1.38/175 (0.0006)	–
3 BB+PL <sup>e</sup>	$2.4^{+1.3}_{-1.2}$	$32^{+7}_{-5}$	$11^{+23}_{-5}$	$125^{+10}_{-9}$	$0.25^{+0.06}_{-0.04}$	$271^{+14}_{-12}$	$0.046^{+0.007}_{-0.006}$	$1.65 \pm 0.24$	$2.1^{+0.9}_{-0.7}$	1.02/173 (0.41)	$2 \times 10^{-12}$
2 Hatm+BB+PL <sup>f</sup>	$3.3^{+1.6}_{-1.3}$	$27^{+5}_{-4}$	10–100	$51 \pm 6$	$4.5^{+2.3}_{-1.7}$	$147^{+11}_{-8}$	$0.4 \pm 0.1$	$1.50 \pm 0.25$	$1.4^{+0.7}_{-0.5}$	1.00/173 (0.48)	–

<sup>a</sup> Power-law normalization in units of  $10^{-5}$  photons  $\text{keV}^{-1} \text{cm}^{-2} \text{s}^{-1}$ .<sup>b</sup>  $f$ -test probability of adding an additional thermal component, obtained by comparing the  $\chi^2$  fit to the fit directly above.<sup>c</sup> Spectral model used: `phabs×powerlaw`.<sup>d</sup> Spectral model used: `phabs×(blackbody+blackbody+powerlaw)`.<sup>e</sup> Spectral model used: `phabs×(blackbody+blackbody+blackbody+powerlaw)`.<sup>f</sup> Spectral model used: `phabs×(blackbody+nsatmos+nsatmos+powerlaw)`. The `nsatmos` components assumed  $R_{\text{NS}}=13.5 \text{ km}$  and  $M_{\text{NS}}=1.44 M_{\odot}$  (see text). The  $R_{\text{eff}}$  values are deduced from the fitted normalization parameters of the `nsatmos` model.**Figure 7.** *XMM*-MOS (black), *NuSTAR*-FPMA (red), *NuSTAR*-FPMB (green) and *ROSAT*-PSPC (blue) unfolded spectra of PSR J0437–4715 fitted with an absorbed triple-blackbody plus power-law model. The addition of the *ROSAT* data permits us to obtain better constraints on the coldest of the three thermal components and on the amount of absorption.

here. An additional multiplicative constant was added to account for the cross-calibration uncertainties of the *ROSAT*-PSPC detectors with *XMM*-MOS and *NuSTAR*-FPMA/B. The combined *ROSAT*-PSPC, *XMM*-MOS and *NuSTAR* spectra could not be adequately fit by a 2BB+PL model ( $p \sim 0.0006$ , see Table 2). The excess emission in the 0.1–0.3 keV band added by the *ROSAT* data was not adequately fitted by the two thermal components and was therefore compensated by a soft PL ( $\Gamma = 2.15^{+0.55}_{-0.20}$ ). This in turn left a large excess of counts in the *NuSTAR* band, causing the observed increase in the  $\chi^2$  statistic.

However, adding a third thermal component confirmed what was observed with the *XMM*-MOS and *NuSTAR* data. Specifically, the 0.1–0.3 keV emission is well fitted by a blackbody with  $kT_{\text{eff}} = 32^{+7}_{-5} \text{ eV}$ . Overall, this leads to an acceptable fit statistic  $\chi^2_{\nu}/\text{dof}$  (prob.) = 1.02/173 (0.41),

and without clear structure in residuals (see Figure 7). Furthermore, while the amount of absorption was unconstrained (upper limit on  $N_{\text{H}}$ ) with the *XMM*-MOS and *NuSTAR* data, the inclusion of the *ROSAT*-PSPC spectrum permitted the measurement of the Galactic absorption,  $N_{\text{H},20} = 2.4^{+1.3}_{-1.2}$ , without ambiguity on the rest of the emission, especially at high energy.

In this spectral analysis, the *XMM*-pn data were not included, since despite their high S/N, they do not significantly improve the constraints on the thermal components. For example, adding the *XMM*-pn data to the *XMM*-MOS and *NuSTAR* spectra resulted in blackbody temperatures  $kT_{\text{eff}} = 117 \pm 6 \text{ eV}$  and  $kT_{\text{eff}} = 254^{+9}_{-8} \text{ eV}$  when fitting a 2BB+PL model. These values are consistent with the *XMM*-MOS/*NuSTAR* spectral fits (see Table 2), but more importantly, the improvements on the statistical uncertainties of the measurements are negligible. Indeed, the timing mode of the *XMM*-pn data has a limited reliable energy range, and requires an additional cross-correlation coefficient (multiplicative constant) which limits the impact of the additional S/N.

### 4.3 Phase-resolved spectral analysis

Using the phase-folded lightcurve presented in Section 3, the on-pulse and off-pulse spectra were extracted (see Figure 1). Because of the limited number of counts in the *NuSTAR* observations of J0437, the analysis was restricted to just two phase bins. Just as performed for the *NuSTAR* data alone, a simple PL model was used for the on- and off-pulse spectra, together with a multiplicative constant accounting for cross-calibration uncertainties. For the on-pulse spectra, a PL photon index  $\Gamma_{\text{on}} = 1.6 \pm 0.3$  was obtained, while the off-pulse photon index was  $\Gamma_{\text{off}} = 1.5 \pm 0.3$ . Both fits are statistically acceptable (null hypothesis probability of  $p \sim 0.2$  and  $p \sim 0.8$ , respectively).

The phase-resolved spectral analysis does not reveal a significant change in the PL index, given the count statistics available. Higher S/N data will be necessary to draw any firm conclusions regarding the variation with phase of the high-energy spectral shape of J0437.



## 5 DISCUSSION AND CONCLUSIONS

Using the well measured radio ephemeris of PSR J0437–4715, pulsations were observed with a significance of  $3.7\sigma$  in a 200 ks *NuSTAR* observation, despite a spin period small enough to potentially be affected by the *NuSTAR* clock drift modulated at the satellite orbital period. Under the assumption that the residual clock drift is sinusoidal over an orbit of the satellite, causing a smearing of the pulse profile, we attempted to recover and correct for a sinusoidal clock drift of unknown phase and amplitude. However, no particular pair of phase and amplitude was found to significantly improve the pulse profile. The measured high energy pulsed fraction of J0437 is  $24 \pm 6\%$  (2–20 keV). When separated into two energy bands, the pulsations are marginally detected, likely due to the low S/N in each band. The pulse fractions ( $32 \pm 9\%$  in 2–6 keV, and  $20 \pm 8\%$  in 6–20 keV) show hints of a decrease with energy, although not significantly. However, it is important to keep in mind that the pulsed fractions of MSPs, like J0437, observed with *NuSTAR* are probably underestimated due to the distortion of the pulse profile by the clock drift. The artificial decrease of the pulse fraction depends on the pulse period and on the magnitude of the clock drift (Figure 3).

The *NuSTAR* observation presented here provided the high-energy constraint needed to remove ambiguities in the soft X-ray spectral modeling. The S/N of previously available spectra was too low above  $\sim 3$  keV to fully characterize the high energy emission. While its presence was confirmed and modeled with a PL in an *XMM-Newton* observation (Bogdanov 2013), the photon index was poorly constrained which resulted in uncertainties in the modeling of the remainder of the soft X-ray emission. We showed that the *NuSTAR* observations alone constrained the photon index of the 3–20 keV emission to  $\Gamma = 1.60 \pm 0.25$ , firmly excluding PL photon indices of  $\sim 2.5$ , as sometimes obtained in fits of the *XMM-Newton* spectra alone (depending on the other spectral components chosen).

With this new high-energy observation, and by comparing the 2BB+PL and 3BB+PL models, we demonstrated that the presence of a third thermal component ( $kT_{\text{BB}} = 32^{+7}_{-5}$  eV) is required by the X-ray emission of J0437. This cold component is thought to be emanate from the entire surface of the NS, while the two hotter thermal components describe the emission from the polar caps of the rotating NS. Such a result is in agreement with the far UV emission which required a NS surface thermal component, since the UV emission could not be accommodated by the white-dwarf atmosphere emission (Durant et al. 2012; Kargaltsev et al. 2004). With the 3BB+PL spectral model, we found a PL index of  $\Gamma = 1.65 \pm 0.24$ .

NS atmosphere models and their beamed emission patterns offer a more realistic representation of the surface thermal emission of NSs than an isotropically radiating Planck spectrum (e.g., Bogdanov et al. 2007). The three Planckian components were therefore replaced by three realistic NS hydrogen atmosphere models (*nsatmos*, Heinke et al. 2006). We found an acceptable fit and a PL index  $\Gamma = 1.46 \pm 0.25$ , consistent with the 3BB+PL case. However, the coldest *nsatmos* has a temperature pegged at the lower limit allowed by the model ( $\log(T/\text{K}) = 5.0$ ), preventing us to properly estimate the errors on the surface temperature. The coldest thermal

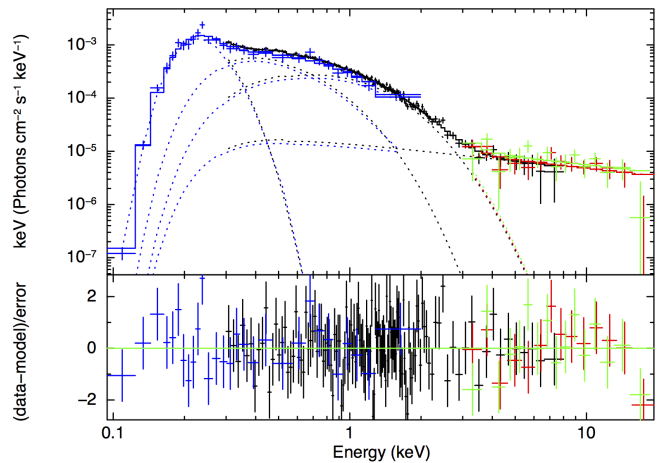


**Figure 8.** *XMM*-MOS (black), *NuSTAR*-FPMA (red), *NuSTAR*-FPMB (green) and *ROSAT*-SPC (blue) unfolded spectra of PSR J0437–4715 fitted with one blackbody, two NS atmosphere *nsatmos* components and a power law, together with a model for Galactic absorption. Replacing the Planck spectral components of Figure 7 by *nsatmos* component does not significantly change the measured PL index, but it increases the contribution of the thermal emission to the flux above 3 keV.

component was replaced by a blackbody component, and we obtained an acceptable fit with a PL index  $\Gamma = 1.50 \pm 0.25$  (see Table 2, for the full set of parameters). Because the high energy tail of NS atmosphere models has slightly more flux than a Planck spectrum (see for example, Zavlin et al. 1996; Heinke et al. 2006; Haakonsen et al. 2012), the PL index measured is slightly harder than that measured in the 3BB+PL case. However, this change is not significant given the S/N available here.

At 6 keV, the hottest blackbody (in the case the 3BB+PL case) is a few orders of magnitude fainter than the PL component (see Figure 7). However, when *nsatmos* models are used, the hottest component contributes to  $\sim 0.3\%$  of the flux at 6 keV (Figure 8) since it falls off less steeply than a blackbody component. Therefore, it cannot be excluded that the pulsed emission below 6 keV is due, in part, to the thermal emission. However, above 6 keV, the pulsed emission is unlikely to originate from the thermal components since its contribution is essentially negligible at 6 keV and above. It is important to keep in mind that the detection significance of the pulsations is marginal when we split the observed photons into low (2–6 keV) and high (6–20 keV) energy bands (see Section 3).

Finally, in the phase-resolved spectroscopic analysis of the *NuSTAR* data, there is no evidence of any significant change in the PL index, most likely due to the low S/N of the spectra obtained when splitting into two phase bins.

When comparing to other non-accreting MSPs<sup>8</sup>, the measured PL of J0437 is consistent with that measured for

<sup>8</sup> We used the list of MSPs detected by *Fermi* (Table 2 of Marelli et al. 2011), as well as other MSPs not detected by *Fermi*, such as PSR B1937–21, and MSPs in the globular clusters 47 Tuc (Bogdanov et al. 2006a) and NGC 6397 (Bogdanov et al. 2010).

most of them. The MSP PSR J1024–0719 has a photon index  $\Gamma = 3.7 \pm 0.8$  when fitted with a single PL model (Zavlin 2006). However, a model with a hot thermal polar cap plus a PL does not provide a constraint on the PL photon index for that MSP. For the MSP PSR B1937+21, the PL photon index is  $\Gamma = 0.9 \pm 0.1$ , and the fit is not significantly improved when adding a thermal component (Ng et al. 2014), providing only an upper limit on the temperature. The MSP PSR J0030+0451 is quite analogous to J0437, and when fitted with two NS atmosphere models plus a PL, the measured photon index is  $\Gamma = 2.0 \pm 0.2$ , consistent with that of J0437, given the uncertainties on both measurements. However, if a single thermal component plus PL model, or two blackbodies plus PL model are chosen, the photon index  $\Gamma = 3.1 \pm 0.1$  is not consistent with that of J0437. This indicates that comparing the PL photon indices of these non-accreting MSPs is rather delicate. In the soft X-ray pass band, the available S/N of these sources is generally rather weak, J0437 (the nearest MSP) being the brightest, which leads to poorly constrained spectral parameters. More importantly, the photon index of the PL components depends strongly on the overall spectral model, and it is frequently found for many X-ray faint MSPs that a blackbody, a PL, or the sum of both, fit the soft X-ray data equally well.

The PL photon index that we found for J0437 is consistent with the photon flux detected by *Fermi* above 0.1 GeV when extending to gamma-ray energies:  $(4.4 \pm 0.1) \times 10^{-8}$  photons cm<sup>-2</sup> s<sup>-1</sup>. However, this may simply be a coincidence since the gamma-ray emission and the hard X-ray non-thermal emission have different origins. Curvature radiation is responsible for the gamma-ray emission (Cheng et al. 1986; Romani 1996; Harding et al. 2008; Lyutikov 2013), while the non-thermal X-ray emission may be due to synchrotron radiation from the shock caused by the interaction of the pulsar wind and its companion wind (Arons & Tavani 1993). However, this possibility would be excluded if the likely pulsations of the non-thermal emission above  $> 6$  keV are confirmed, since synchrotron radiation would not produce pulsed emission. Furthermore, it had been shown that the non-thermal X-ray emission of J0437 is lower than what would be expected from a shock given the binary system orbital properties (Bogdanov et al. 2006b). The proposed alternative interpretation of the non-thermal emission involves electrons and positrons in the pulsar magnetosphere causing the weak Comptonization of the thermal photons (Bogdanov et al. 2006b). This interpretation could explain that the non-thermal emission of J0437 is likely pulsed as observed in the present work. However, the existence of such pulsations would depend on the viewing geometry, and on the location from which scattered photons originate. Such information could be extracted from a higher S/N pulse profile at energies above 6 keV where the thermal emission is negligible.

The non-thermal emission characterized in this work confirms what had been observed in a previous work where a PL with  $\Gamma = 1.56$  matches both the *XMM* emission  $\lesssim 8$  keV and at *Fermi* energies (Figure 13 of Durant et al. 2012). Furthermore, when extended to UV energies, the PL emission complements the “cold” surface emission to fit the UV emission detected by the *Hubble Space Telescope* (Durant et al. 2012). The present *NuSTAR* observation and the measurements of the PL photon index shed light on the broadband

emission of J0437, confirming that the non-thermal emission is likely to extend over many decades of energy. Furthermore, knowledge of the non-thermal emission allowed us to constrain the temperature of the NS cold surface emission as well as the amount of X-ray absorption (described by  $N_H$ ). Therefore, it favours the cut-PL model (with a cut-off at  $\sim 1.1$  GeV), rather than a variable PL model (Durant et al. 2012).

Overall, a global understanding of the broadband emission of J0437, and in particular a clear characterization of its thermal emission, are crucial to extract the mass and radius of the pulsar. J0437 is the key target for observations with *NICER*, a NASA experiment to be mounted on the International Space Station circa 2017. The modeling of the pulse profiles and of the spectral emission obtained from combining 1 Msec of observations with *NICER* is expected to produce stringent constraints on the compactness of J0437 ( $M_{\text{NS}}/R_{\text{NS}}$ ). Since the mass of the pulsar is known from radio timing observations, combining the X-ray and radio measurements of  $M_{\text{NS}}$  and  $R_{\text{NS}}$  would result in tight constraints in the mass-radius parameter space, and therefore in stringent constraints on the dense matter equation of state (Gendreau et al. 2012). However, such an analysis requires a full understanding of the emission in the *NICER* passband, i.e. 0.2–10 keV.

It is difficult to estimate quantitatively how this *NuSTAR* observation will improve the  $M_{\text{NS}}/R_{\text{NS}}$  measurements that can be derived from currently available *XMM* data, and from future *NICER* data. Specifically, it is unclear how the characterization of the non-thermal emission that was performed in the present work will affect the modeling of the pulse profile. Nevertheless, in the previous work, the contribution of the non-thermal emission was included as an un-pulsed contribution with a  $\Gamma = 1.56$  PL spectrum (Bogdanov 2013). While we confirm here that the PL index is consistent with  $\Gamma = 1.56$ , we also demonstrated that the non-thermal emission is probably pulsed, although this requires higher S/N observations to be confirmed with higher certainty. This is particularly important above 6 keV where the hot thermal component is more than two orders of magnitude fainter and therefore does not contribute to the pulsations. Consequently, *NuSTAR* provides information regarding the likely pulsed behaviour of the non-thermal emission of J0437. While no change in the PL index was detected between the on- and off- pulse parts of the profiles, the varying flux of the non-thermal emission as a function of phase ought to be included in the modeling of the full pulse profile.

Even up to 3 keV (the upper limit of the range available for the currently available *XMM*-pn data), the PL contributes to the phase-averaged flux (Figure 8), and therefore contribute to the overall pulsed emission observed in the *XMM* data. Note that in our best-fit model with *nsatmos* thermal components, the PL contribution to the flux becomes larger than that of the hot thermal component at around  $\sim 2.7$  keV (Figure 8). By neglecting the pulsed emission of the PL, one will attribute more pulsed flux to the thermal components than in reality. As a direct consequence of this, the best-fit geometry of the model or the measured NS compactness could be biased.

Confirming the existence of the third (coldest) thermal component and measuring the temperature of the surface emission of J0437 is also of great importance to confirm

the existence of reheating mechanisms in old NSs. Standard cooling models predict surface temperatures of  $< 10^4$  K after  $10^9$  yr. However, evidence of a  $\sim 10^5$  K surface temperature for J0437 despite its characteristic age  $> 10^8$  yr indicates that reheating mechanisms might be at play inside old NSs (for example, rotochemical heating, or frictional heating, see [Gonzalez & Reisenegger 2010](#), for more details). However, the present work used a blackbody to fit the coldest thermal component, while a realistic atmosphere model with a range of temperature compatible with  $T < 10^5$  K should be used. In addition, measurements of the UV fluxes of J0437 (e.g.: [Durant et al. 2012](#)) can be used to help constrain that coldest thermal component since the Rayleigh-Jeans tail is detected in the UV and Far UV range (Gonzalez-Caniulef, Reisenegger & Guillot, in prep.).

In conclusion, future pulse profile and phase resolved spectral modeling of J0437, in particular those of future *NICER* data, must take into account the likely pulsed non-thermal emission with a photon index of  $\Gamma = 1.50 \pm 0.25$ . Ideally, the emission above  $\sim 3$  keV should be divided into more phase bins for a more accurate determination of the non-thermal emission of J0437 as a function of phase. However, this would require higher S/N data, and therefore deeper exposures with *NuSTAR*.

**Acknowledgements** The authors thank the referee, Slavko Bogdanov, for very useful suggestions that significantly improved this paper. This work made use of data from the *NuSTAR* mission, a project led by the California Institute of Technology, managed by the Jet Propulsion Laboratory, and funded by the National Aeronautics and Space Administration. The data analysis was performed with the *NuSTAR* Data Analysis Software (NuSTARDAS) jointly developed by the ASI Science Data Center (ASDC, Italy) and the California Institute of Technology (USA). S.G. is a FONDECYT post-doctoral fellow, funded by grant # 3150428. VMK receives support from an NSERC Discovery Grant and Accelerator Supplement, from the Centre de Recherche en Astrophysique du Québec, an R. Howard Webster Foundation Fellowship from the Canadian Institute for Advanced Study, the Canada Research Chairs Program and the Lorne Trottier Chair in Astrophysics and Cosmology. Parts of this research were conducted by the Australian Research Council Centre of Excellence for All-sky Astrophysics (CAASTRO), through project number CE110001020.

## REFERENCES

Abdo A. A., et al., 2009, *Science*, **325**, 848  
 An H., et al., 2015, *ApJ*, **807**, 93  
 Arons J., Tavani M., 1993, *ApJ*, **403**, 249  
 Balucinska-Church M., McCammon D., 1992, *ApJ*, **400**, 699  
 Becker W., Trümper J., 1993, *Nat.*, **365**, 528  
 Bogdanov S., 2013, *ApJ*, **762**, 96  
 Bogdanov S., Grindlay J. E., Heinke C. O., Camilo F., Freire P. C. C., Becker W., 2006a, *ApJ*, **646**, 1104  
 Bogdanov S., Grindlay J. E., Rybicki G. B., 2006b, *ApJL*, **648**, L55  
 Bogdanov S., Rybicki G. B., Grindlay J. E., 2007, *ApJ*, **670**, 668  
 Bogdanov S., Grindlay J. E., Rybicki G. B., 2008, *ApJ*, **689**, 407  
 Bogdanov S., van den Berg M., Heinke C. O., Cohn H. N., Lugger P. M., Grindlay J. E., 2010, *ApJ*, **709**, 241  
 Cheng K. S., Ho C., Ruderman M., 1986, *ApJ*, **300**, 522

Deller A. T., Verbiest J. P. W., Tingay S. J., Bailes M., 2008, *ApJL*, **685**, L67  
 Durant M., Kargaltsev O., Pavlov G. G., Kowalski P. M., Posselt B., van Kerkwijk M. H., Kaplan D. L., 2012, *ApJ*, **746**, 6  
 Edwards R. T., Hobbs G. B., Manchester R. N., 2006, *M.N.R.A.S.*, **372**, 1549  
 Gendreau K. C., Arzoumanian Z., Okajima T., 2012, in Society of Photo-Optical Instrumentation Engineers (SPIE) Conference Series. , doi:10.1117/12.926396  
 Gonzalez D., Reisenegger A., 2010, *A&A*, **522**, A16  
 Guillot S., Rutledge R. E., 2014, *ApJL*, **796**, L3  
 Guillot S., Rutledge R. E., Brown E. F., Pavlov G. G., Zavlin V. E., 2011, *ApJ*, **738**, 129  
 Guillot S., Servillat M., Webb N. A., Rutledge R. E., 2013, *ApJ*, **772**, 7  
 Güver T., Özel F., Cabrera-Lavers A., Wroblewski P., 2010, *ApJ*, **712**, 964  
 Haakonsen C. B., Turner M. L., Tacik N. A., Rutledge R. E., 2012, *ApJ*, **749**, 52  
 Halpern J. P., Martin C., Marshall H. L., 1996, *ApJL*, **473**, L37  
 Harding A. K., Stern J. V., Dyks J., Frackowiak M., 2008, *ApJ*, **680**, 1378  
 Harrison F. A., et al., 2013, *ApJ*, **770**, 103  
 Heinke C. O., 2013, *Journal of Physics Conference Series*, **432**, 012001  
 Heinke C. O., Rybicki G. B., Narayan R., Grindlay J. E., 2006, *ApJ*, **644**, 1090  
 Heinke C. O., et al., 2014, *M.N.R.A.S.*, **444**, 443  
 Johnston S., et al., 1993, *Nat.*, **361**, 613  
 Kargaltsev O., Pavlov G. G., Romani R. W., 2004, *ApJ*, **602**, 327  
 Kaspi V. M., Roberts M. S. E., Harding A. K., 2006, Isolated neutron stars. pp 279–339, doi:10.2277/0521826594  
 Krimm H. A., et al., 2013, *ApJ Supp.*, **209**, 14  
 Lattimer J. M., Prakash M., 2007, *Phys. Rep.*, **442**, 109  
 Lyutikov M., 2013, *M.N.R.A.S.*, **431**, 2580  
 Madsen K. K., et al., 2015, *ApJ Supp.*, **220**, 8  
 Marelli M., De Luca A., Caraveo P. A., 2011, *ApJ*, **733**, 82  
 Miller M. C., 2013, preprint, ([arXiv:1312.0029](#))  
 Ng C.-Y., Takata J., Leung G. C. K., Cheng K. S., Philippopoulos P., 2014, *ApJ*, **787**, 167  
 Özel F., Psaltis D., 2009, *Ph.Rev.D*, **80**, 103003  
 Özel F., Psaltis D., Güver T., Baym G., Heinke C., Guillot S., 2016, *ApJ*, **820**, 28  
 Reardon D. J., et al., 2016, *M.N.R.A.S.*, **455**, 1751  
 Romani R. W., 1996, *ApJ*, **470**, 469  
 Suleimanov V., Poutanen J., Revnivtsev M., Werner K., 2011, *ApJ*, **742**, 122  
 Verbiest J. P. W., et al., 2008, *ApJ*, **679**, 675  
 Webb N. A., Barret D., 2007, *ApJ*, **671**, 727  
 Wijnands R., van der Klis M., 1998, *Nat.*, **394**, 344  
 Wilms J., Allen A., McCray R., 2000, *ApJ*, **542**, 914  
 Winkler C., et al., 2003, *A&A*, **411**, L1  
 Zavlin V. E., 2006, *ApJ*, **638**, 951  
 Zavlin V. E., Pavlov G. G., Shibano Y. A., 1996, *A&A*, **315**, 141  
 Zavlin V. E., Pavlov G. G., Sanwal D., Manchester R. N., Trümper J., Halpern J. P., Becker W., 2002, *ApJ*, **569**, 894  
 de Jager O. C., Raubenheimer B. C., Swanepoel J. W. H., 1989, *A&A*, **221**, 180

## APPENDIX A: PSR J0437–4715 EPHEMERIS

We provide in Table A1 of this appendix the parameters of the ephemeris obtained from data collected at the Molonglo observatory between March 2005 and February 2011.

**Table A1.** Molonglo ephemeris of PSR J0437–4715.  $1\sigma$  uncertainties on the last digit of each parameters are represented in parantheses.

Parameter	Value
Right ascension $\alpha$ (J2000)	04 37 15.8961749(7)
Declination $\delta$ (J2000)	-47 15 09.11071(1)
Proper motion in $\alpha$ (mas/yr)	121.428(4)
Proper motion in $\delta$ (mas/yr)	-71.473(5)
Annual parallax (mas)	6.28 (11)
Pulse period (ms)	5.757451936712643(3)
Pulse period derivative ( $10^{-20}$ )	5.72918(1)
Orbital period (days)	5.7410480(9)
Orbital period derivative ( $10^{-12}$ )	3.75(4)
Epoch of periastron passage (MJD)	54530.1724(3)
Projected semi-major axis (s)	3.36671468(5)
Orbital eccentricity ( $10^{-5}$ )	1.917974290(1)
Longitude of periastron ( $^{\circ}$ )	1.37(2)
Periastron advance ( $^{\circ}$ /yr)	0.022(4)
Longitude of ascension ( $^{\circ}$ )	207(1)
Orbital inclination ( $^{\circ}$ )	137.55(5)
Reference epoch (MJD)	54500
MJD Range	53431.26–55619.19